

THE [Fe II]1.644 μ M EMISSION IN M82 AND NGC 253: IS IT A MEASURE OF THE SUPERNOVA RATE?^a

^aBASED ON OBSERVATIONS WITH THE NASA/ESA HUBBLE SPACE TELESCOPE, OBTAINED AT THE SPACE TELESCOPE SCIENCE INSTITUTE, WHICH IS OPERATED BY THE ASSOCIATION OF UNIVERSITIES FOR RESEARCH IN ASTRONOMY, INC. UNDER NASA CONTRACT NO. NAS5-26555.

ALMUDENA ALONSO-HERRERO, GEORGE H. RIEKE, MARCIA J. RIEKE AND DOUGLAS M. KELLY

Steward Observatory, The University of Arizona, Tucson, AZ 85721

Draft version November 10, 2018

ABSTRACT

We present *HST*/NICMOS [Fe II]1.644 μ m, Pa α (1.87 μ m) and continuum images of the starburst galaxies M82 and NGC 253 at an unprecedented spatial resolution. In both galaxies we detect [Fe II] compact sources superimposed on a diffuse background in the disk of the galaxies together with a component above and below the plane of the galaxy. The radio and [Fe II] emissions perpendicular to the disk of M82 show a remarkable similarity to each other, suggesting that both emissions originate in shocks from supernova explosions. We find a spatial correspondence between bright compact [Fe II] emitting regions and the location of radio supernova remnants (SNR) for approximately 30 – 50% of radio SNRs in M82 and NGC 253. This lack of a one-to-one correspondence, more than being indicative of a different origin for the radio and [Fe II] emission in starbursts, suggests two populations of SNRs: an older population ($\lesssim 10^4$ yr) traced by the [Fe II] emission and a younger population (a few hundred years old) traced by the radio SNRs. We therefore conclude that the [Fe II] emission in starburst galaxies provides a good estimate of the supernova activity. Using our newly determined [Fe II] luminosities (corrected for extinction) of M82 and NGC 253, we reevaluate the calibration of the supernova rate in terms of the [Fe II] luminosity for starburst galaxies.

Subject headings: Galaxies: individual: M82, NGC 253 – galaxies: nuclei – galaxies: photometry – infrared: galaxies

1. INTRODUCTION

Compact radio sources in nearby starburst galaxies often appear to be supernova remnants (SNR). SNR in our Galaxy and the Large Magellanic Cloud (LMC) are sources of bright near-infrared [Fe II] line emission with luminosities ranging from 10^{26} W to 3×10^{29} W (for the [Fe II]1.644 μ m line, e.g., Oliva, Moorwood, & Danziger 1989; Burton & Spyromilio 1993). This behavior suggests a connection between supernova activity and the [Fe II] emission in starbursts. This is supported by near-infrared spectroscopy (Moorwood & Oliva 1988; Greenhouse et al. 1991; Vanzi & Rieke 1997), by high-resolution [Fe II] imaging studies (Forbes et al. 1993; Greenhouse et al. 1997; Alonso-Herrero et al. 2000), and by the tight correlation between the radio 6 cm and the [Fe II] emissions (Forbes & Ward 1993). Further determination of the relation of the infrared [Fe II] emission with the supernova activity in nearby starforming galaxies would be helpful both for the understanding of these galaxies and for using the near-infrared [Fe II] luminosity as estimator of the supernova rate in more distant galaxies where individual radio supernovae cannot be identified.

There are indications of some complexities in this relation. For example, the bright [Fe II] emission may not be spatially coincident with the radio SNR. Lumsden & Puxley (1995) conducted a spectroscopic survey for [Fe II] emission from radio SNRs in M33 and found that in some cases the [Fe II] emission does not peak at the position of the radio SNR, as well as that some radio SNR show no [Fe II] emission. Recently, Morel, Doyon, & St-Louis (2002)

have carried out an [Fe II] imaging survey of optically selected SNR in M33 and found a similar result. Both works have concluded that the [Fe II] emission from SNR may be produced over a time scale of $\sim 10^4$ years. Greenhouse et al. (1997) found that none of the brightest sources of [Fe II] emission in M82 were coincident with the position of the radio SNRs.

M82 and NGC 253 are the nearest starburst galaxies (distances $d = 3.2$ Mpc and $d = 2.5$ Mpc respectively). Both galaxies show a large number of radio compact sources (e.g., $\simeq 50$ in M82 Kronberg et al. 1985 and Huang et al. 1994; $\simeq 60$ in NGC 253 Turner & Ho 1985 and Ulvestad & Antonucci 1991, 1997 and references therein). Their proximity makes these two galaxies ideal to study the relation between supernova activity and the [Fe II] emission in starburst galaxies. Greenhouse et al. (1997) presented a Fabry-Perot [Fe II]1.644 μ m map for M82 with a spatial resolution of $\simeq 1.3''$. Their main conclusions were that the compact [Fe II] sources contribute only $\simeq 14\%$ of the total [Fe II] emission in M82 and that they trace a population of SNR older than the radio SNR. Their work is somewhat inconclusive because of the limited angular resolution and also because strong extinction could hide [Fe II] emission from some of the radio SNRs. This paper presents *HST*/NICMOS images of M82 and NGC 253. The high spatial resolution of the NICMOS [Fe II]1.644 μ m images (FWHM = $0.35''$; this corresponds to 5 pc and 4 pc for M82 and NGC 253, respectively) allows a detailed study of the location of the bright sources of [Fe II] and of the rôle of supernova remnants in this line emission.

2. NICMOS OBSERVATIONS

2.1. Data Reduction

HST/NICMOS observations were obtained on April 7, 8, 12 and 22 1998 (for M82) and on August 13 and 20 1998 (for NGC 253) using the NIC2 and NIC3 cameras. Table 1 lists details of the observations. The observational strategy consisted of taking images in a spiral dither with a 5.5 pixel spacing with four positions for a given field. The plate scales for the NIC2 and NIC3 cameras are $0.076'' \text{ pixel}^{-1}$ and $0.20'' \text{ pixel}^{-1}$, respectively. The FWHM of the point sources in the NIC3 F166N continuum images is $0.35''$.

The reduction of the NICMOS images used routines from the package *NicRed* (McLeod 1997). A master dark image was produced by combining between 10 and 20 darks for a given sample sequence after the subtraction of the first readout. The darks used were part of other proposals observed close in time, and the flatfield images were on-orbit data. The data reduction was performed using the following steps: subtraction of the first readout, dark current subtraction on a readout basis, correction for linearity and cosmic ray rejection (using *fullfit*), and flatfielding. The individual dithered galaxy images were registered to a common position using fractional pixel offsets and cubic spline interpolation, and combined to produce the final image of each field.

2.2. Flux-calibration of the images

Prior to the flux calibration of the images, the background needs to be subtracted (only for wavelengths longwards of $2 \mu\text{m}$). Due to the large projected size of both galaxies, the field of view of the NIC2 images is not large enough to enable measurements of the background on empty corners of the images, so we used background measurements taken during the Servicing Mission Observatory Verification (SMOV) program for the filter NIC2 F222M. The F215N images cover a larger field of view, and an estimate of the thermal background was obtained from the corners of the images. The flux calibration of the broad-band, on-line and off-line images was performed using the conversion factors (from ADU/s to mJy) based on measurements of the standard star P330-E during SMOV (Marcia Rieke 1999 private communication).

Ideally one would like to measure the continuum on both sides of the emission line to estimate the continuum at the emission line. However, NICMOS only provides continuum bands to the red of the emission line. In cases of objects such as M82 and NGC 253, where the extinction to the nuclear regions is very high (even at infrared wavelengths), a straight subtraction of the longer wavelength off-line image may result in an over correction of the continuum at the wavelength of the emission line. To estimate the continuum for the NIC3 F164N images, we fitted the continuum on a pixel-by-pixel basis between $1.66 \mu\text{m}$ and $2.15 \mu\text{m}$ by linear regression of the flux as a function of the wavelength for the NIC3 F166N and NIC3 F215N line-free images. The extrapolated continuum was then subtracted from the NIC3 F164N image to produce the final continuum-subtracted [Fe II] $1.644 \mu\text{m}$ line image. This procedure does not correct for extinction, but it rather ensures the subtraction of the correct *obscured* continuum at each position of the galaxy. For the NIC2 F187N image (Pa α), since we did not have other narrow-band images

taken with camera 2, we used the NIC2 F190N continuum image. Fortunately, the continuum need not be subtracted as accurately for Pa α as for the [Fe II] emission line because the Pa α emission is much brighter.

The fully-reduced images of each individual field were combined to produce the mosaics. The images presented in this paper were taken during different orbits. This resulted in slightly different orientations (from P.A. = -100° to -105° for M82 and from P.A. = 57° to 68° for NGC 253). Before combining the images into mosaics, they were rotated by linear interpolation to north up, east to the left. This provided the same orientation for all the images, and more importantly allows comparisons with previously published data.

To construct extinction maps to correct the [Fe II] emission, and [Fe II]/Pa α maps, the NIC2 F187N, F190N, F160W and F222M images were demagnified to match the plate scale of the NIC3 images and filtered with a Gaussian with $\sigma = 0.65 \text{ pixel} = 0.13''$ to match the point spread function (PSF) of the NIC3 images.

3. THE [Fe II] $1.644 \mu\text{m}$ AND PA α MORPHOLOGIES

3.1. M82

Figure 1a and 1b are mosaics (after rotation) of the continuum at $1.66 \mu\text{m}$ and the continuum-subtracted [Fe II] $1.644 \mu\text{m}$ line emission, respectively. Both images are displayed on a logarithmic scale to stress the contrast between the diffuse extended continuum and the compact sources. The [Fe II] $1.644 \mu\text{m}$ line map has been smoothed with a Gaussian filter with $\sigma = 0.1''$. The line emission image shows some residuals which are due to both the under-sampling of the NIC3 camera PSF and the variation in the shape of the PSF with wavelength. In addition, the right hand side of the line image shows a slightly lower S/N because the F164N and F166N images at that position had different orientations.

The [Fe II] $1.644 \mu\text{m}$ line emission exhibits two distinct components: a number of relatively compact regions distributed along the disk of the galaxy and an extended diffuse component in the form of filaments extending above and below the plane of the galaxy. The filaments seen in the [Fe II] $1.644 \mu\text{m}$ emission line show a remarkable similarity with the chimneys at the base of the superwind detected in radio (Wills et al. 1999), which are interpreted by these authors as expelled material from the central region of M82.

In Figures 2a and 2b we present contour maps of the $1.66 \mu\text{m}$ continuum emission and the [Fe II] $1.644 \mu\text{m}$ line emission, respectively. Comparison of the NICMOS [Fe II] $1.644 \mu\text{m}$ line map with that of Greenhouse et al. (1997) reveals that some of the sources seen in the lower resolution map of Greenhouse et al. (1997) break up into individual sources at higher spatial resolution. In particular, their source Fe1 contains some 4 or 5 individual sources. Source Fe6 (the most south-west source in Greenhouse et al. 1997 map) appears as a point source at our resolution in both the NIC3 F164N and NIC3 F166N images, and the signal to noise on it is compromised by the differing image orientations (see above). Therefore it is not surprising we do not detect line emission from it. The NICMOS images detect a number of compact sources in addition to those reported in Greenhouse et al. (1997).

TABLE 1
LOG OF THE HST/NICMOS OBSERVATIONS.

Camera (1)	Filter (2)	line/filter (3)	galaxy (4)	t_{exp} (5)	no. fields (6)	field of view (7)
NIC2	F160W	H	M82	192	4	$29.2'' \times 72.7''$
			NGC 253	192	2	$26.3'' \times 33.1''$
NIC2	F222M	K	M82	448	4	$29.2'' \times 72.7''$
			NGC 253	512	2	$26.3'' \times 33.1''$
NIC2	F187N	$\text{Pa}\alpha$	M82	384	4	$29.2'' \times 72.7''$
			NGC 253	384	2	$26.3'' \times 33.1''$
NIC2	F190N	continuum	M82	384	4	$29.2'' \times 72.7''$
			NGC 253	384	2	$26.3'' \times 33.1''$
NIC3	F164N	$[\text{Fe II}]1.644 \mu\text{m}$	M82	4096	2	$53.8'' \times 66.2''$
			NGC 253	2560	1	$51.2'' \times 51.2''$
NIC3	F166N	continuum	M82	3840	2	$53.8'' \times 66.2''$
			NGC 253	2560	1	$51.2'' \times 51.2''$
NIC3	F215N	continuum	M82	2304	2	$53.8'' \times 66.2''$
			NGC 253	2304	1	$51.2'' \times 51.2''$

NOTE.—Column (1): NICMOS camera. Column (2): Filter. Column (3): Corresponding ground-based broad-band filter, emission line or adjacent continuum. Column (4): Galaxy. Column (5): total integration time per field. Column (6): Number of fields observed to produce the final mosaic image. Column (7): Field of view of the mosaic before rotation to the common orientation of north up, east to the left.

In Figures 2a and 2b we display the positions of 44 radio SNRs with peak flux densities above 1 mJy (list provided by Dr. Karen Wills, see more details in Section 5.1). The distribution of the radio SNRs and their relation with the $[\text{Fe II}]1.644 \mu\text{m}$ emission will be discussed in Section 5.

In Figures 3a and 3b we display the mosaics of the $1.90 \mu\text{m}$ continuum (NIC2 F190N images) and the $\text{Pa}\alpha$ line emission (continuum subtracted NIC2 F187N images) respectively. The $\text{Pa}\alpha$ image is dominated by a ring of ionized gas with an approximate diameter of 400 pc. The resemblance with the mid-infrared $[\text{Ne II}]$ line emission map at $12.8 \mu\text{m}$ (Achtermann & Lacy 1995) is remarkable. The south side of this ring of ionized material appears to be incomplete (see Achtermann & Lacy 1995), and it also shows a “hole” of emission at the center of the galaxy, which approximately coincides with the peak of the $2.2 \mu\text{m}$ surface brightness.

It has been suggested that higher extinction in the south half of M82 may be causing the uneven distribution of ionized gas in the ring. However, the ring appears to be complete in $[\text{Fe II}]1.644 \mu\text{m}$ line emission. If extinction were the cause, we should expect to see a similar morphology in the $[\text{Fe II}]$ emission, which is more affected by extinction than the $\text{Pa}\alpha$ emission. It is therefore tempting to suggest that the south part of the ring of ionized gas is actually *broken*, perhaps due to SN explosions. This hypothesis would also explain the excess of $[\text{Fe II}]$ emission in this region. The presence of the hole of gas emission at the center of M82 along with the anti-correlation between the morphology of the hydrogen recombination lines and the CO index has been invoked as evidence for an outwards propagating starburst (e.g., Satyapal et al. 1997). The diffuse component of $\text{Pa}\alpha$ emission is also in the form of “fingers” or “filaments” above and below the plane of the galaxy. It is now known from ground-based $\text{H}\alpha$ imaging that this

emission along the minor axis of the galaxy extends over 11 kpc (Devine & Bally 1999). Figure 1b and Figure 3b show how there is a very close spatial correspondence between the morphologies of the extended $[\text{Fe II}]1.644 \mu\text{m}$ and $\text{Pa}\alpha$ emissions.

3.2. NGC 253

Figures 4a and 4b are the $1.66 \mu\text{m}$ continuum and the $[\text{Fe II}]1.644 \mu\text{m}$ line emission maps of NGC 253. As seen in M82, the $[\text{Fe II}]1.644 \mu\text{m}$ emission is in the form of a number of compact regions along the disk of the galaxy superimposed on a diffuse emission component. Figures 5a and 5b are contour plots of these two emissions. We also show the positions of the 6 cm radio sources with $S_{\text{peak}} > 1 \text{ mJy}$ from Ulvestad & Antonucci (1991), excluding those sources that are classified as H II regions in Ulvestad & Antonucci (1997).

Ground-based $[\text{Fe II}]1.644 \mu\text{m}$ and $\text{Br}\gamma$ maps at lower spatial resolution (FWHM $\simeq 1.3''$) were previously observed by Forbes et al. (1993). They found that the central $[\text{Fe II}]$ emission of NGC 253 is dominated by three peaks of emission. Our higher resolution NICMOS image shows a larger number of $[\text{Fe II}]$ compact sources. For instance, source B (in the Forbes et al. 1993 notation) breaks up into three individual sources. In addition to the nucleus and sources A and B detected by Forbes et al. (1993), there are other sources along the disk of the galaxy, as well as diffuse emission perpendicular to the disk, more prominent in the south half of the galaxy. We believe that Forbes et al. (1993) did not detect the diffuse component above and below the disk of the galaxy because of the lower S/N of their $[\text{Fe II}]$ map. We also mark in these figures the position of the peak (the filled square) of the near-infrared emission (also coincident with the peak of the $\text{Pa}\alpha$ emission) which was identified as the nucleus of

TABLE 2
EXTINCTION TO THE NUCLEAR REGIONS OF M82 USING A FOREGROUND DUST SCREEN MODEL.

Ratio: flux(1)/flux(2)	Ap.	flux(1)	flux(2)	A_V	References flux(1), flux(2)
Emission line measurements					
	($''$)	($W m^{-2}$)	($W m^{-2}$)	(mag)	
P α /H α	5.8	5.30×10^{-15}	2.80×10^{-15}	5 ± 0.5	this work, O'Connell & Mangano (1978)
P α /P $\alpha\beta$	6	5.30×10^{-15}	5.90×10^{-16}	11 ± 1	this work, McLeod et al. (1993)
P α /P $\alpha\gamma$	3	1.27×10^{-15}	0.5×10^{-16}	10 ± 1	this work, McLeod et al. (1993)
P α /P $\alpha\beta$	3	1.27×10^{-15}	1.47×10^{-16}	11 ± 1	this work, McLeod et al. (1993)
Br γ /P α	3.8	2.00×10^{-16}	2.08×10^{-15}	11 ± 4	Lester et al. (1991), this work
Br α /P α (E1)	6?	4.55×10^{-15}	4.65×10^{-15}	18 ± 3	Achtermann & Lacy (1995), this work
Br α /P α (W1)	6?	3.92×10^{-15}	5.92×10^{-15}	13 ± 2	Achtermann & Lacy (1995), this work
Br α /P α (W2)	6?	7.30×10^{-15}	5.12×10^{-15}	23 ± 3	Achtermann & Lacy (1995), this work
[Fe II]1.64/[Fe II]1.25	3	9.20×10^{-17}	5.20×10^{-17}	10 ± 1	this work, McLeod et al. (1993)
Continuum measurements					
	($''$)	(mJy)	(mJy)	(mag)	
F222M/F160W	3	237	166	13 ± 2	this work

NOTE.—Apertures are circular and centered at the peak of the $2.2 \mu m$ continuum brightness, except for sources E1, W1 and W2 in Achtermann & Lacy (1995) notation. The approximate locations of the Br α (or P α) sources from the peak of the near-infrared emission are: E1 ($+4.1''$, $+0.5''$), W1 ($-4.6''$, $-2.0''$) and W2 ($-10.3''$, $-4.5''$). The errors quoted for the extinctions include uncertainties from the aperture size and centering, and flux calibration.

TABLE 3
EXTINCTION TO THE NUCLEAR REGIONS OF NGC 253 USING A FOREGROUND DUST SCREEN MODEL.

Ratio: flux(1)/flux(2)	Ap.	flux(1)	flux(2)	A_V	References flux(1), flux(2)
Emission line measurements					
	($''$)	($W m^{-2}$)	($W m^{-2}$)	(mag)	
P α /Br γ (center)	$3'' \times 3''$	1.58×10^{-15}	1.41×10^{-16}	5 ± 7	this work, Harrison et al. (1998)
P α /Br γ (center)	$3.9'' \times 4.8''$	2.40×10^{-15}	2.35×10^{-16}	11 ± 6	this work, Puxley & Brand (1995)
P α /Br γ ($3''$ NE)	$3'' \times 3''$	1.20×10^{-15}	1.15×10^{-16}	8 ± 12	this work, Harrison et al. (1998)
P α /Br γ ($3.9''$ NE)	$3.9'' \times 4.8''$	2.00×10^{-15}	1.83×10^{-16}	7 ± 12	this work, Puxley & Brand (1995)
Continuum measurements					
	($''$)	(mJy)	(mJy)	(mag)	
F222M/F160W (center)	$3.9'' \times 4.8''$	213	142	13 ± 2	this work

NOTE.—Apertures are rectangular, and centered at the peak of the $2.2 \mu m$ continuum brightness (center) and at the P α source located NE of the continuum peak. The errors in the derived extinctions take into account 10% and 20% uncertainties for the nucleus and NE source measurements, respectively.

the galaxy by Forbes et al. (1993). Other authors (e.g., Keto et al. 1999) claim that a bright non-thermal radio source located NE of the peak of the infrared continuum emission (source 2 in Turner & Ho 1985) may be the true nucleus of NGC 253. It is shown in these figures as a filled star symbol.

The NICMOS Pa α line map (Figure 6b) shows very bright emission stemming from the peak of infrared continuum emission, together with more diffuse emission in a plume-like morphology along the plane of the galaxy, primarily to the NE of the nucleus. As for M82, there is an extended component of the Pa α emission perpendicular to the disk, better seen in our NIC3 images (not shown here) which are more sensitive to diffuse emission. This component is however not as strong as that in M82. There is a remarkable resemblance of the central Pa α emission with both the [Ne II]12.8 μ m emission line and the nearby continuum images presented in Böker, Krabbe, & Storey (1998) and Keto et al. (1999).

4. EXTINCTION

Both M82 and NGC 253 are known to be highly obscured (see for instance the comparison between the optical *HST*/WFPC2 F555W and the *HST*/NICMOS F222M images of M82 in Alonso-Herrero et al. 2001). To calibrate the supernova rate in terms of the [Fe II]1.644 μ m emission and to obtain the total number of ionizing photons, it is necessary to correct the observed quantities for extinction.

4.1. M82

We can estimate the extinction to the gas in M82 using observations of the ratios of hydrogen recombination and near-infrared [Fe II] lines. We used published values of the line fluxes for the smallest apertures and matched those apertures on the NICMOS line images when measuring the Pa α and [Fe II]1.644 μ m fluxes. The intrinsic ratios of hydrogen recombination lines are from Hummer & Storey (1987) for an electron temperature of $T_e = 10^4$ K and electron density of $n_e = 10^4$ cm $^{-3}$. The ratio between [Fe II]1.257 μ m and [Fe II]1.644 μ m does not depend upon the physical conditions of the gas. We used a polynomial fit to the near-infrared extinction law given in He et al. (1995).

Since we do not have NICMOS images of two hydrogen recombination lines, to measure extinction at the full NICMOS angular resolution we made use of the broadband filters NIC2 F160W and NIC2 F222M to construct a map of extinction to the stars in M82. We assumed a color for the unreddened stellar population of $H - K = 0.2$ (which applies almost independently of the age of the population), and, for computational convenience, a foreground dust screen model following the extinction law of He et al. (1995). The contribution of dust emission at the K -band was assumed to be negligible. Figure 7a is the extinction map (A_K) from the $H - K$ color map of M82, with the positions of the radio sources superimposed. The values of the extinction in the K -band derived from this map are between $A_K = 0.3$ mag and $A_K = 2.5$ mag. The M82 extinction map qualitatively looks very similar to those of Satyapal et al. (1995), but quantitatively the values of the extinction are different.

The estimates of the extinction to the gas for M82 are presented in the first part of Table 2 along with the

line fluxes. The errors in Table 2 are the uncertainties associated with the aperture size, aperture centering and flux calibration. For comparison, we also estimated the extinction through a small aperture (3'') using the F222M/F160W continuum flux ratio, which gives an estimate of the visual extinction to the stars. As can be seen from this table the agreement between the extinctions to the gas and to the stars is excellent at infrared wavelengths. Satyapal et al. (1995) reached a similar conclusion. A much lower level of extinction is indicated by comparing the H α and Pa α line fluxes. This behavior is known to arise from the different optical depths probed by optical and near-infrared lines. This behavior is confirmed by the much higher extinction of $A_V \simeq 27$ mag inferred by Puxley et al. (1989) from the radio H53 α to mid-infrared Br α line ratio.

We also computed the extinctions to the E1, W1 and W2 regions in Achtermann & Lacy (1995) notation (see Table 2 for the positions). These were found to be bright in [Ne II]12.8 μ m and Br α . We used their Br α measurements along with the mid-infrared extinction curve in Rieke & Lebofsky (1985). Since Achtermann & Lacy (1995) did not quote aperture sizes, we assumed that their fluxes were measured over the extent of these regions (approximately 5'' - 6'' in diameter). The values of the extinction for these three regions are slightly larger than the values we would measure from the $H - K$ extinction map, perhaps indicating minor differences in the optical depth.

A further test of the extinction to the gas was based on the total number of ionizing photons from the extinction corrected Pa α line emission map. The number of ionizing photons obtained from the extinction-free H53 α radio recombination line is $N_{Ly} = 1 \times 10^{54}$ s $^{-1}$ (Puxley et al. 1989), and from the 3.3 mm continuum is $N_{Ly} = 1.1 \times 10^{54}$ s $^{-1}$ (Carlstrom & Kronberg 1991). We measured through a large aperture the Pa α flux on the observed and the extinction-corrected images. We obtained $N_{Ly} = 4 \times 10^{53}$ s $^{-1}$ (observed) and $N_{Ly} = 1.4 \times 10^{54}$ s $^{-1}$ (corrected for extinction), for electron temperature $T_e = 10^4$ K. The total number of ionizing photons corrected for extinction is in excellent agreement with a number of estimates including those of Puxley et al. (1989), Carlstrom & Kronberg (1991) and Förster Schreiber et al. (2001).

4.2. NGC 253

As for M82, the extinction to the stars was computed from the $H - K$ color map of NGC 253 (Figure 7b). It shows values between $A_V = 3$ mag and $A_V = 21$ mag and is very similar to that of Sams et al. (1994) derived from a $J - K$ color map. We find a similar value of the extinction ($A_V \simeq 21$ mag) for the point with the highest value of the extinction which was identified by Sams et al. (1994) as the true nucleus of NGC 253.

To calculate the extinction to the gas in NGC 253 we used Pa α and Br γ fluxes (the latter from Puxley & Brand 1995 and Harrison et al. 1998). Both works centered their apertures on the approximate coordinates of the secondary near-infrared peak and therefore we will assume that the largest Br γ fluxes in these works correspond to the primary near-infrared peak. If their (0,0) position were to be identified with the peak of the continuum emission, their fluxes would not be consistent with Forbes et al. (1993) Br γ line

emission map. This map and our Pa α line emission map (Figure 6b) show that the brightest hydrogen line emission arises from the peak of the continuum emission. In Table 3 we give estimates for the extinction for the primary near-infrared peak (center) and secondary near-infrared peak (positions 3'' and 3.9'' to the NE of the primary peak for Puxley & Brand 1995 and Harrison et al. 1998 works respectively). The errors take into account 10% and 20% combined flux calibration/centering uncertainties for the nucleus and NE source, respectively.

The values of the gas extinction to these two regions as derived from the Pa α /Br γ line ratio are consistent (to within the errors) with the extinction to the stars from the $H - K$ color map. Despite this apparent good agreement we caution the reader of the aforementioned centering uncertainties. We also measured the observed and corrected for extinction Pa α fluxes which yielded a number of ionizing photons of $N_{Ly} = 2.5 \times 10^{52} \text{ s}^{-1}$ (observed) and $N_{Ly} = 1.4 \times 10^{53} \text{ s}^{-1}$ (corrected for extinction), for the field of view shown in Figure 6b. The latter value is consistent with Engelbracht et al. (1998) and Keto et al. (1999) estimates of the number of ionizing photons from their large aperture Br γ and [Ne II] measurements, but smaller than Puxley et al. (1997) estimate ($N_{Ly} = 3.7 \times 10^{53} \text{ s}^{-1}$) from millimeter-wavelength hydrogen recombination lines.

5. THE [Fe II] 1.644 μM EMISSION OF M82 AND NGC 253

5.1. The Distribution of the [Fe II] 1.644 μm and radio SNRs

To determine whether there is a spatial correspondence between the compact radio sources and the [Fe II] sources in both M82 and NGC 253, very precise coordinates are needed. Unfortunately, due to problems with the *HST* telemetry during the observations of M82, and the uncertainties when producing and rotating the mosaics, the coordinates of the NIC3 images may not be completely reliable. In addition, it is expected that there are minor discrepancies between the radio and the optical/infrared coordinate reference systems.

Our approach was to determine the coordinates of the [Fe II] image by trying to find the highest possible number of coincidences between the positions of the radio SNRs and the [Fe II] sources. We use DAOFIND within the DAOPHOT package in IRAF to find compact sources. The term ‘‘compact’’ is not used in the sense of point sources. In fact, most of these sources seem to be slightly resolved, although due to the under-sampling of the NIC3 PSF, some uncertainties remain. The sources were selected to be easily distinguishable from the extended diffuse emission detected above and below the plane of the galaxy.

In M82 we identified 65 ‘‘compact’’ sources in the [Fe II] 1.644 μm map (not corrected for extinction). For the radio sources in M82 we used the positions of SNRs identified by searching for compact features within radio maps at 408 MHz, 1.4 GHz, 5 GHz and 8.4 GHz, with peak flux densities above 1 mJy (Dr. Karen Wills, private communication 2000). We excluded from this list radio sources that are classified as H II regions based on their radio spectral index (see McDonald et al. 2002 for details), resulting in 44 radio SNRs. We began the comparison of positions

using the coordinates in the header of the NICMOS NIC3 F164N images and made small offsets of the [Fe II] image, cross-correlating the positions of the [Fe II] sources with the radio SNRs. Based on the resolution of the NIC3 images and the average angular size of the radio SNRs ($\simeq 0.2''$, Huang et al. 1994), we counted a coincidence when the angular separation between a radio source and an [Fe II] source was $\leq 0.5''$. With a small shift, we found 21 coincidences between radio SNRs and [Fe II] sources, whereas if we used the original coordinates we could only find 7 coincidences. Monte Carlo simulations showed that the probability of finding 21 coincidences by pure chance is 2×10^{-6} (see Whitmore & Zhang 2002 for details on the method), so we believe that now the infrared and the radio images are properly aligned.

For NGC 253 we found discrepancies between the coordinates derived for the near-infrared peak of emission from the NIC2 and NIC3 images (which were taken during two different orbits). Although no problems were reported for these two sets of observations, some error must be affecting the coordinates given in the headers of the images. Again as with M82, we cross-correlated the positions of the [Fe II] 1.644 μm (36 sources) and 35 radio sources taken from Ulvestad & Antonucci 1991 — excluding those sources that are classified as H II regions in Ulvestad & Antonucci (1997) — using the coordinates of the NIC3 images. We find a total of 9 coincidences for a separation between the radio sources and [Fe II] sources $\leq 0.5''$. The probability of finding 9 coincidences in by pure chance in NGC 253 is approximately 9×10^{-3} .

One important conclusion, despite the uncertainties of the image alignment, is that we cannot assign an [Fe II] source to each radio SNR or vice versa. We find approximately 30 – 50% of radio SNRs in M82 and NGC 253 have an [Fe II]. This point is illustrated in the contour images of the [Fe II] 1.644 μm line emission and continuum emission at 1.66 μm in Figures 2a and 2b for M82 and Figures 5a and 5b for NGC 253. In all figures we show the positions of the radio SNRs as asterisks.

We also tried to determine if there is a relation between the presence of a coincidence and the age of the radio SNR. Such a correlation would be expected if the [Fe II] emission were brighter in older supernova remnants. For M82 we used the angular sizes of the radio SNR as an indication of their age (see Huang et al. 1994). In general, we did not find that older radio SNRs tend to have a coincidence with an [Fe II] source.

5.2. Luminosity and Origin of the [Fe II] 1.644 μm sources

5.2.1. Supernova Excitation

We performed aperture photometry on the [Fe II] sources identified in M82¹ and NGC 253 using a fixed 0.8'' diameter aperture. This aperture corresponds to a physical size of 12 pc and 10 pc for M82 and NGC 253, respectively. Figures 9a and 9b show the distributions of the measured [Fe II] 1.644 μm luminosities (not corrected for extinction). Some of the sources may be larger than the aperture used for the photometry; on the other hand, patchy extinction will make some of the sources appear smaller. From inspection of typical source sizes, however, the luminosities

¹Since the photometry was done on the [Fe II] image registered to match the field of view and position of the Pa α image, the number of detected sources (71) is slightly different from that in Section 5.1

would be accurate on average. Recent studies of Galactic SNR show that the [Fe II] emission is filamentary and have sizes of the order of 11 pc (e.g. IC443 Rho et al. 2001; see also Morel et al. 2002 for SNR in M33).

For the assumed distances to M82 and NGC 253 the observed [Fe II]1.644 μm luminosities of these sources range from 2.2×10^{27} W to 1.2×10^{30} W. As a consistency check for the photometry, we measured the [Fe II]1.644 μm fluxes for the Fe1, Fe2 and Fe3 sources in M82 identified by Greenhouse et al. (1997) using the aperture diameters listed in their table 1. The agreement with Greenhouse et al. (1997) fluxes for these sources is excellent, to within 3%. However, when we compared our photometry for the sources reported in Forbes et al. (1993) for NGC 253 we found some discrepancies.

The corrected [Fe II]1.644 μm luminosities for compact sources in M82 and NGC 253 range from 3×10^{29} W to 2.2×10^{31} W. As a comparison, Galactic SNRs yield [Fe II]1.644 μm luminosities of 1×10^{26} W to 7×10^{28} W (Oliva et al. 1989; Keller et al. 1995), SNRs in the LMC yield luminosities from 1×10^{28} W to 3×10^{29} W (Oliva et al. 1989) and SNRs in M33 (assuming a distance of 720 kpc) 5×10^{27} to 3×10^{29} W (Lumsden & Puxley 1995 and Morel et al 2002).

The individual sources account for some 22% and 27% of the total [Fe II]1.644 μm emission (extinction corrected) measured in M82 and NGC 253, respectively. Given the estimates that the [Fe II] emitting phase of a SNR has a duration of $\simeq 10^4$ yr (Lumsden & Puxley 1995; Morel et al. 2002) and the supernova rates in M82 and NGC 253 are $\simeq 0.10 \text{ yr}^{-1}$ (Huang et al. 1994 and Ulvestad & Antonucci 1997), the detected [Fe II] sources account for $\simeq 1000$ yr worth of supernovae. Presumably much of the remaining unresolved [Fe II] arises from additional supernovae that are packed so densely that they are confused in our images. Also, SNRs in these two galaxies may expand and merge into a general hot ISM within a few thousand years losing their identity as individual sources. Photometry on the [Fe II] emission arising from the disk of M82 shows that as much as 70% of the total emission (disk plus component perpendicular to the disk) is associated with SNRs. This together with the good agreement between the radio and [Fe II] morphologies of the components perpendicular to the disk gives further indication for a SNR origin of the [Fe II] emission in starburst galaxies.

Lumsden & Puxley (1995) pointed out that one possibility is that the [Fe II] lines reach maximum luminosity when the remnant as a whole undergoes the transition from adiabatic expansion to radiative expansion. According to Shull & Draine (1986), this happens when radiative cooling occurs faster than dynamical times, around 10^4 yr after the supernova explosion. Therefore if the brightest [Fe II] emission occurs at approximately 10^4 yr, it is not surprising that we do not find a correspondence for all the [Fe II] sources and all the radio SNRs. Muxlow et al. (1994) found that half of the radio sources in M82 are unresolved indicative of a young age, but the other resolved half are probably intermediate age. This together with the fact that we found that 30 – 50% of the radio SNR have an [Fe II] counterpart implies that the [Fe II] sources may be $\lesssim 10^4$ yr.

5.2.2. Excitation in H II Regions

One possibility for the lack of one-to-one coincidences between the radio SNRs and the [Fe II] sources would be that most of the [Fe II] emission in these two galaxies is produced in H II regions (photoionization). To check this, we measured the Pa α fluxes for the sources detected in the [Fe II] extinction corrected map of M82, and assumed an [Fe II]1.644 μm /Pa α ratio for H II regions as that observed in Orion. We found that only $\simeq 6 - 8\%$ of the total [Fe II]1.644 μm arises from H II regions. This further supports the hypothesis that most of the [Fe II]1.644 μm emission along the plane of M82 is produced by SNRs.

The [Fe II]/Br γ ratios in H II regions and SNR differ by a factor of a hundred or more, and therefore can be used to indicate the excitation mechanism of the [Fe II] line within our images. In Alonso-Herrero et al. (1997) we showed that the behavior of the [Fe II]1.644 μm /Br γ line ratio in starbursts and active galaxies can be understood as a progression from pure photoionization to pure shock excitation going from pure H II regions through starbursts, transition objects, Seyferts to supernova remnants.

Figures 8a and 8b are the observed [Fe II]1.644 μm /Pa α maps for M82 and NGC 253, respectively. The values of the [Fe II]1.644 μm /Pa α ratio range from 0.02 in black (mostly along the disk of the galaxy) to 0.8 in white (some of the bright [Fe II] sources). These ratios translate into [Fe II]1.644 μm /Br γ line ratios of between 0.24 and 10 (see also the histograms in Figure 10). Since these maps are not corrected for extinction, these numbers are actually lower limits. When the positions of radio sources are plotted in the [Fe II]1.644 μm /Pa α maps we find again that there is a number of coincidences between the radio SNRs and the regions of enhanced [Fe II]1.644 μm emission. This indicates that the relative contribution of the SNRs is nearly as large in the diffuse background as it is in the radio SNR. Interestingly, we find that most of the coincidences with the radio SNRs occur in regions of enhanced [Fe II]1.644 μm /Pa α line ratio, or conversely we do not find a large number of coincidences in regions with high Pa α flux (that is, H II regions).

6. CALIBRATION OF THE SUPERNOVA RATE – [FE II] LUMINOSITY RELATION

The supernova rate in M82 has been estimated from number counts of the radio supernova remnants and their ages to be $0.11 \pm 0.05 \text{ yr}^{-1}$ (Huang et al. 1994). The total [Fe II]1.644 μm luminosity in M82 is $L([\text{Fe II}]_{\text{total}}) = 1.9 \times 10^{33}$ W. Our value for the [Fe II] luminosity of M82 is approximately 1.5 and 2 times higher than the previous estimates by Greenhouse et al. (1997) and Vanzi & Rieke (1997), respectively. This difference is most likely due to better extinction estimates made possible by our NICMOS images. If the supernova rate in M82 is 0.11 yr^{-1} , then we can derive the following calibration for the supernova rate in terms of the [Fe II]1.644 μm luminosity:

$$(\text{SNR})_{\text{M82}} = 0.6 \times \frac{L_{[\text{Fe II}]}}{10^{34} \text{ W}} \quad (\text{yr}^{-1}) \quad (1)$$

The total [Fe II]1.644 μm luminosity (corrected for extinction) measured in NGC 253 is 6.1×10^{32} W. An upper limit on the supernova rate from radio supernova counts is $< 0.1 - 0.3 \text{ yr}^{-1}$ (Ulvestad & Antonucci 1997). A rate of 0.08 yr^{-1} has been calculated assuming that the non-thermal radio flux is entirely due to synchrotron emission

(Van Buren & Greenhouse 1994); this value is consistent with the similar number of compact radio sources in this galaxy compared with M82. The calibration of supernova rate in terms of [Fe II]1.644 μm luminosity for this galaxy is then

$$(\text{SNr})_{\text{NGC253}} = 1.3 \times \frac{L_{[\text{Fe II}]}}{10^{34}\text{W}} \text{ (yr}^{-1}\text{)} \quad (2)$$

Since M82 is the more thoroughly studied galaxy in the radio, we give higher weight to the calibration for it in averaging these results to estimate

$$(\text{SNr}) = 0.8 \times \frac{L_{[\text{Fe II}]}}{10^{34}\text{W}} \text{ (yr}^{-1}\text{)} \quad (3)$$

In the above calculations, we have included the entire [Fe II] luminosity, since that is the parameter usually measured in a distant galaxy. However, in these nearby examples, we can compare the [Fe II] emission produced in H II regions with that from supernovae. We assume that the ratio for a typical H II region is $f([\text{Fe II}]1.644 \mu\text{m})_{\text{HII}} \simeq 6.6 \times 10^{-3} f(\text{Pa}\alpha)$ (e.g., Orion). We obtained that the [Fe II] luminosity produced in H II regions accounts for less than 8% the total [Fe II] luminosity in M82.

7. SUMMARY AND CONCLUSIONS

We have presented *HST*/NICMOS observations of the starburst galaxies M82 and NGC 253. The morphology of the [Fe II]1.644 μm line emission in both galaxies displays two components: (1) a disk component with a number of superimposed compact sources and (2) a diffuse component in the form of filaments above and below the disk of the galaxy. In M82 we find a remarkable similarity between the extended component, the fingers or chimneys above and below the disk, of the radio and [Fe II] emissions.

In M82, we have detected in both Pa α and [Fe II] a nuclear ring of star formation. This ring, with an approximate diameter of 400 pc, has also been observed in other near- and mid-infrared hydrogen recombination lines and in the [Ne II]12.8 μm line. The peak of the 2.2 μm continuum brightness of M82 lies very close to (within 1'') the dynamical center, and corresponds to the center of the ring of star formation. In NGC 253, bright Pa α emission stems from the near-infrared continuum peak and extends in a plume-like morphology along the disk of the galaxy. There is also a diffuse Pa α component above and below the plane of galaxy, however, much fainter than that in M82.

Prior to calibrating the supernova rate in terms of the [Fe II] emission, we have derived the extinction to the cen-

tral regions of NGC 253 and M82. To assess the extinction correction, we have compared the number of ionizing photons inferred from the extinction-corrected Pa α maps with other estimates based on longer wavelength indicators, and found a good agreement.

Since the [Fe II] emission in starburst galaxies is thought to be associated with supernova activity, we have cross-correlated the positions (with a spatial resolution of a few tenths of arcseconds) of the radio SNRs and the identified compact [Fe II] sources in M82 and NGC 253. We have found that approximately 30 – 50% of the radio SNRs have an [Fe II] counterpart. However, we cannot associate an [Fe II] source to each radio SNR or vice versa. This is well understood in terms of the different ages traced by the radio SNRs (a few hundred years) and the [Fe II] stage of SNRs ($\lesssim 10^4$ yr). The compact [Fe II] emitting sources in M82 and NGC 253 only contribute to some 20 – 30% of the total [Fe II]1.644 μm emission. However, much of the remaining emission in the disk of the two galaxies is most likely produced by SNRs that expanded and merged into a general ISM a few 10^4 yr ago. Photometry on the [Fe II]1.644 μm emission arising from the disk of M82 shows that as much as 70% of the total [Fe II]1.644 μm emission (corrected for extinction) is associated with SNRs. The remaining diffuse [Fe II] emission perpendicular to the disk of M82 seems to be related to the superwind (via expulsion of material from the central starburst), as argued from the radio emission morphology (Wills et al. 1999).

All these arguments support the supernova origin for the observed near-infrared [Fe II] line emission in starburst galaxies. Thus we have recalibrated the supernova rate in terms of the [Fe II] luminosity relation for starburst galaxies using our newly measured (corrected for extinction) [Fe II]1.644 μm luminosities of M82 and NGC 253.

ACKNOWLEDGMENTS

We would like to thank Drs. Karen Wills, T. Muxlow and A. Pedlar for kindly providing us with the radio images for comparison with the NICMOS images, and the list of radio SNR. We are also grateful to Dr. Ernesto Oliva for enlightening discussions, and an anonymous referee for constructive comments that helped improve the paper.

During the course of this work AA-H was supported by the National Aeronautics and Space Administration on grant NAG 5-3042 through the University of Arizona. The work was also partially supported by the National Science Foundation under grant AST-95-29190.

REFERENCES

- Achtermann, J. M., & Lacy, J. H. 1995, *ApJ*, 439, 163
 Alonso-Herrero, A., Rieke, M. J., Rieke, G. H., & Ruiz, M. 1997, *ApJ*, 482, 747
 Alonso-Herrero, A., Rieke, G. H., Rieke, M. J., & Scoville, N. Z. 2000, *ApJ*, 532, 845
 Alonso-Herrero, A., Rieke, M. J., Rieke, G. H., & Kelly, D. M. 2001, *Ap&SS*, 276, 1109
 Böker, T., Krabbe, A., & Storey, J. W. V. 1998, *ApJ*, 498, L115
 Burton, M. & Spyromilio, J. 1993, *PASAu*, 10, 327
 Carlstrom, J. E., & Kronberg, P. P. 1991, *ApJ*, 366, 422
 Engelbracht, C. W., Rieke, M. J., Rieke, G. H., Kelly, D. M., & Achtermann, J. M. 1998, *ApJ*, 505, 639
 Forbes, D. A., Ward, M. J., Rotaciuc, V., Blietz, M., Genzel, R., Drapatz, S., van der Werf, P., & Krabbe, A. 1993, *ApJ*, 406, L11
 Forbes, D. A., & Ward, M. J. 1993, *ApJ*, 416, 150
 Förster Schreiber, N. M., Genzel, R., Lutz, D., Kunze, D., & Sternberg, A. 2001, *ApJ*, 552, 544
 Greenhouse, M. A., Woodward, C. E., Thronson, H. A. Jr., Rudy, R. J., Rossano, G. S., Erwin, P., & Puetter, R. C. 1991, *ApJ*, 383, 164
 Greenhouse, M. A., Satyapal, S., Woodward, C. E., Fisher, J., Thompson, K. L., Forrest, W. J., Pipher, J. L., Raines, N., Smith, H. A., Watson, D. M., & Rudy, R. J. 1997, *ApJ*, 476, 105
 Harrison, A., Puxley, P., Russell, A., & Brand, P. 1998, *MNRAS*, 297, 624
 He, L., Whittet, D. C. B., Kilkenny, D., Spencer Jones, J. H. 1995, *ApJS*, 101, 335

- Huang, Z. P., Thuan, T. X., Chevalier, R. A., Condon, J. J., & Yin, Q. F. 1994, *ApJ*, 424, 114
- Hummer, D. G., & Storey, P. J. 1987, *MNRAS*, 224, 801
- Keller, L. D., Jaffe, D. T., Pak, S., Luhman, M. L., & Claver, C. F. 1995, *Rev. RMxAC*, 3, 251
- Keto, E., Hora, J. L., Fazio, G. G., Hoffmann, W., & Deutsch, L. 1999, *ApJ*, 518, 183
- Kronberg, P. P., Biermann, P., & Schwab, F. R. 1985, *ApJ*, 291, 693
- Lester, D. F., Carr, J. S., Joy, M., & Gaffney, N. 1990, *ApJ*, 352, 544
- Lumsden, S. L., & Puxley, P. J. 1995, *MNRAS*, 276, 723
- McDonald, A. R., Muxlow, T. W. B., Kills, K. A., Pedlar, A., & Beswick, R. J. 2002, *MNRAS*, 334, 912
- McLeod, B. 1997 in *HST Calibration Workshop*, ed. S. Casertano, R. Jedrzejewski, T. Keyes, and M. Stevens, published by the Space Telescope Science Institute, Baltimore, MD, p. 281
- McLeod, K. K., Rieke, G. H., Rieke, M. J., & Kelly, D. M. 1993, *ApJ*, 412, 111
- Moorwood, A. F. M., & Oliva, E. 1988, *A&A*, 203, 278
- Morel, T., Doyon, R., & St-Louis, N. 2002, *MNRAS*, 329, 398
- Muxlow, T. W. B., Pedlar, A., Wilkinson, P. N., Axon, D. J., Sanders, E. M., & de Bruyn, A. G. 1994, *MNRAS*, 266, 455
- O'Connell, R. W., & Mangano, J. J. 1978, *ApJ*, 221, 62
- Oliva, E., Moorwood, A. F. M., & Danziger, I. J. 1989, *A&A*, 214, 307
- Puxley, P. J., Mountain, C. M., Brand, P. W. J. L., Moore, T. J. T., & Nakai, N. 1997, *ApJ*, 485, 143
- Puxley, P. J., & Brand, P. W. J. L. 1995, *MNRAS*, 274, L77
- Puxley, P. J., Brand, P. W. J. L., Moore, T. J. T., Mountain, C. M., Nakai, N., & Yamashita, T. 1989, *ApJ*, 345, 163
- Rho, J., Jarrett, T. H., Cutri, R. M., & Reach, W. T. 2001, *ApJ*, 547, 885
- Rieke, G. H., & Lebofsky, M. J. 1985, *ApJ*, 288, 618
- Sams, B. J. III, Genzel, R., Eckart, A., Tacconi-Garman, L., & Hofmann, R. 1994, *ApJ*, 430, L33
- Satyapal, S., Watson, D. M., Pipher, J. L., Forrest, W. J., Coppenbarger, D., Raines, S. N., Libonate, S., Piché, F., Greenhouse, M. A., Smith, H. A., Thompson, K. L., Fisher, J., Woodward, C. E., & Hodge, T. 1995, *ApJ*, 448, 611
- Satyapal, S., Watson, D. M., Pipher, J. L., Forrest, W. J., Greenhouse, M. A., Smith, H. A., Fisher, J., & Woodward, C. E. 1997, *ApJ*, 483, 148
- Shull, J. M., & Draine, B. T. 1986, in *Interstellar Processes*, ed. D. J. Hollenbach and H. A. Thronson, Jr., p.283
- Turner, J. L., & Ho, P. T. P. 1985, *ApJ*, 299, L77
- Ulvestad, J. S., & Antonucci, R. R. J. 1991, *AJ*, 102, 875
- Ulvestad, J. S., & Antonucci, R. R. J. 1997, *ApJ*, 488, 621
- Van Buren, D., & Greenhouse, M. A. 1994, *ApJ*, 431, 640
- Vanzi, L., & Rieke, G. H. 1997, *ApJ*, 479, 694
- Whitmore, B. C., & Zhang, Q. 2002, *AJ*, 124, 1418
- Wills, K. A., Redman, M. P., Muxlow, T. W. B., & Pedlar, A. 1999, *MNRAS*, 309, 395

figure1a.jpeg

FIG. 1A.— M82: continuum emission at $1.66 \mu\text{m}$ (NIC3 F166N image), displayed on a logarithmic scale.

figure1b.jpeg

FIG. 1B.— M82: [Fe II] $1.644 \mu\text{m}$ line emission (continuum subtracted NIC3 F164N image), displayed on a logarithmic scale.

FIG. 2A.— Contour map of the M82 continuum emission at $1.66 \mu\text{m}$ on a linear scale. The asterisks are the positions of the radio SNRs detected in radio maps (Karen Wills, private communication 2000, see text for details).

FIG. 2B.— Contour map of the M82 [Fe II]1.644 μm line emission (continuum subtracted) on a linear scale. Symbols as in Figure 2a.

figure3b.jpeg

FIG. 3A.— M82: continuum emission at 1.90 μm (NIC2 F190N images) displayed on a logarithmic scale.

figure3b.jpeg

FIG. 3B.— M82: Pa α (1.87 μm) line emission map (continuum subtracted NIC2 F187N images) displayed on a logarithmic scale.

figure4a.jpeg

FIG. 4A.— NGC 253: continuum emission at 1.66 μm (NIC3 F166N image), displayed on a logarithmic scale.

figure4b.jpeg

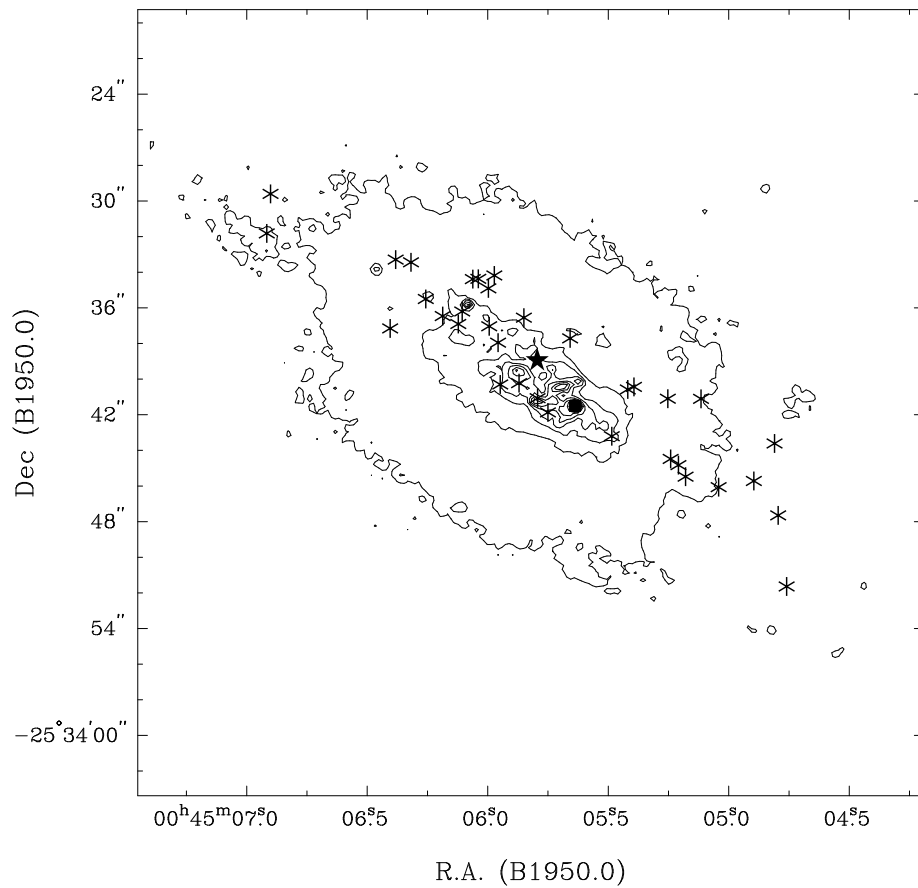
FIG. 4B.— NGC 253: [Fe II]1.644 μm line emission (continuum subtracted NIC3 F164N image), displayed on a logarithmic scale.

FIG. 5A.— Contour map of the NGC 253 continuum emission at 1.66 μm on a linear scale. The asterisks are the positions of the 6 cm radio SNRs from Ulvestad & Antonucci (1991) with $S_{\text{peak}} > 1 \text{ mJy}$, excluding those sources classified as H II regions in Ulvestad & Antonucci (1997). The filled triangle is the position of the peak of the near-infrared emission, whereas the filled star symbol is the position of the non-thermal radio source (see text for details).

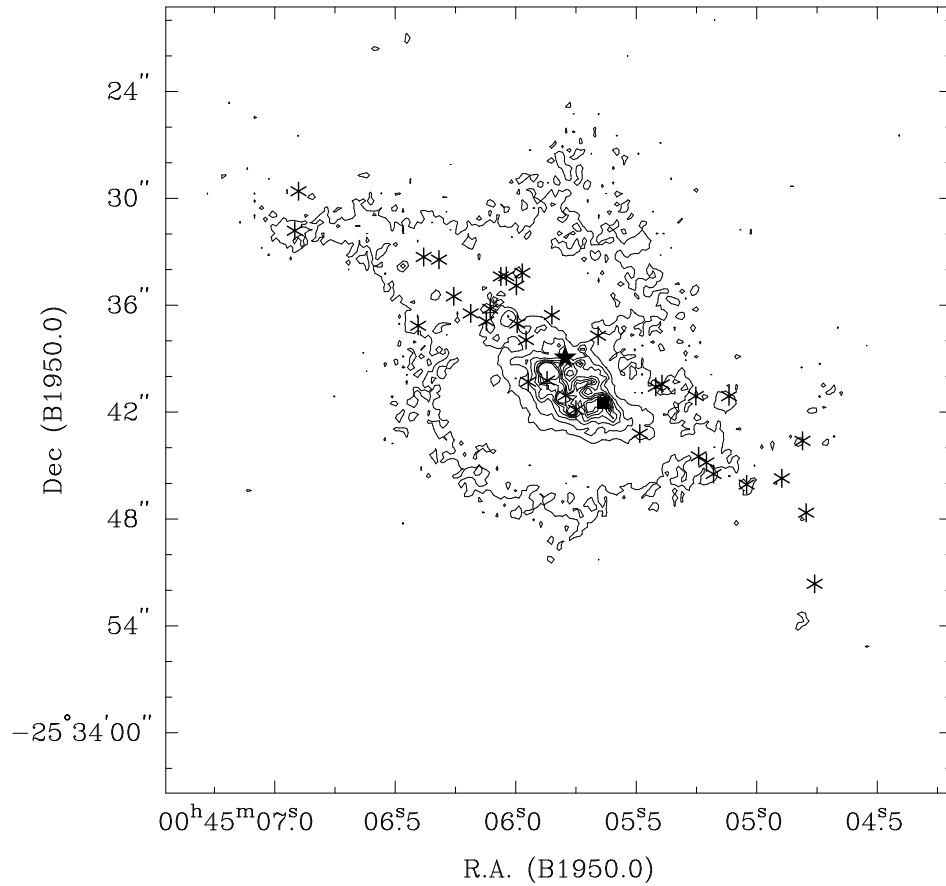


FIG. 5B.— Contour map of the NGC 253 [Fe II] $1.644 \mu\text{m}$ line emission (continuum subtracted) on a linear scale. Symbols as in Figure 5a.

figure6a.jpeg

FIG. 6A.— NGC 253: continuum emission at $1.90 \mu\text{m}$ (NIC2 F190N images) displayed on a logarithmic scale.

figure6b.jpeg

FIG. 6B.— NGC 253: $\text{Pa}\alpha$ ($1.87 \mu\text{m}$) line emission map (continuum subtracted NIC2 F187N images) displayed on a logarithmic scale.

figure7a.jpeg

FIG. 7A.— M82: $H - K$ color map (NIC2 F160W - NIC2 F222M) which represents the extinction to the stars. Symbols are as in Figure 2a. Dark regions indicate regions of higher extinction. The circular black spot on the upper right corners of the individual images is the coronagraphic hole.

figure7b.jpeg

FIG. 7B.— NGC 253: $H - K$ color map (NIC2 F160W - NIC2 F222M). Symbols are as in Figure 5a. The black spot on left bottom corners of the individual images is the coronagraphic hole.

figure8a.jpeg

FIG. 8A.— M82: [Fe II]1.644 μm /Pa α line ratio map. Lighter colors indicate regions of enhanced [Fe II]1.644 μm /Pa α line ratios. Superimposed are the positions of the radio SNRs as in Figure 2a.

figure8b.jpeg

FIG. 8B.— NGC 253 [Fe II]1.644 μm /Pa α line ratio map. Colors as in Figure 8a. Superimposed are the positions of the radio SNRs as in Figure 5a.

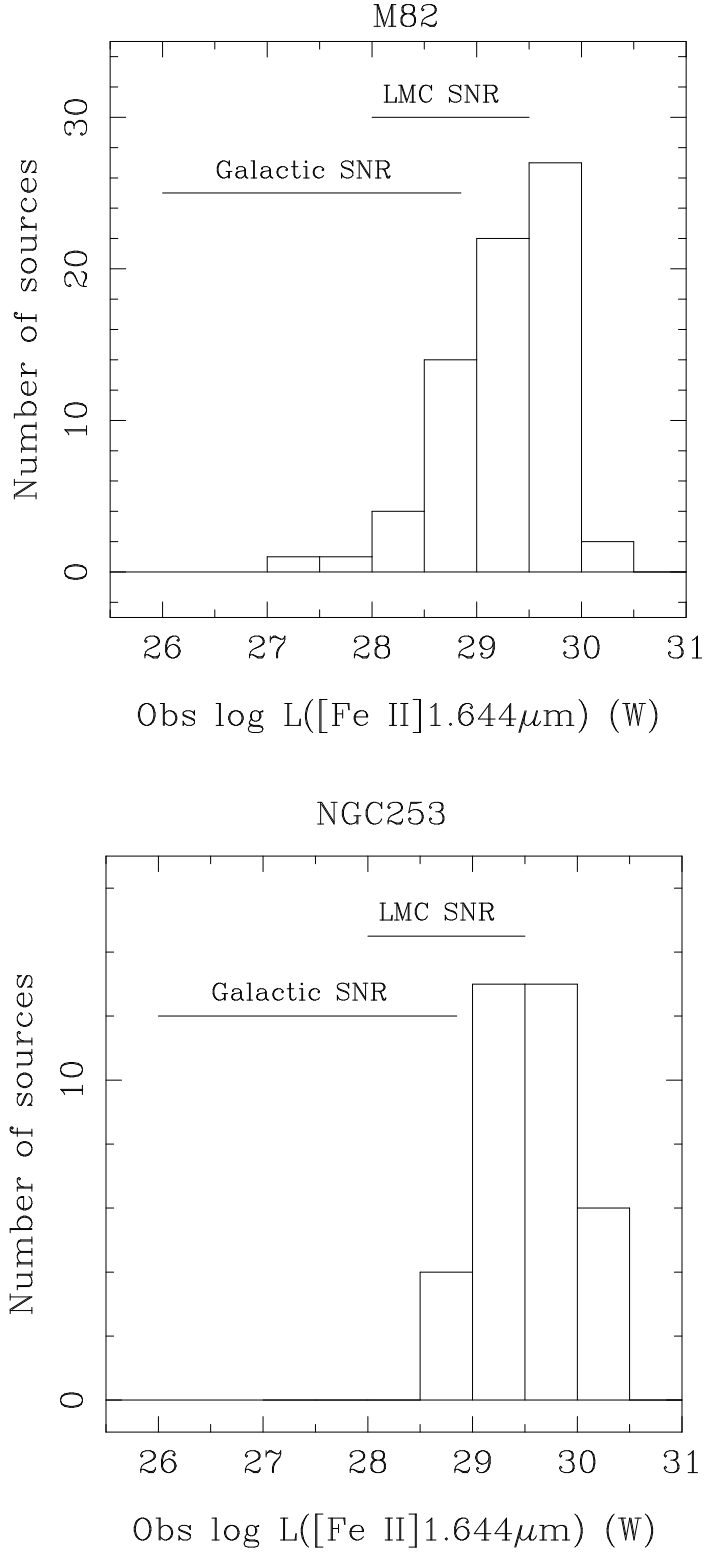


FIG. 9.— Distributions of the [Fe II]1.644 μ m luminosities (not corrected for extinction) of the compact sources in M82 and NGC 253 measured through a 0.8'' diameter aperture.

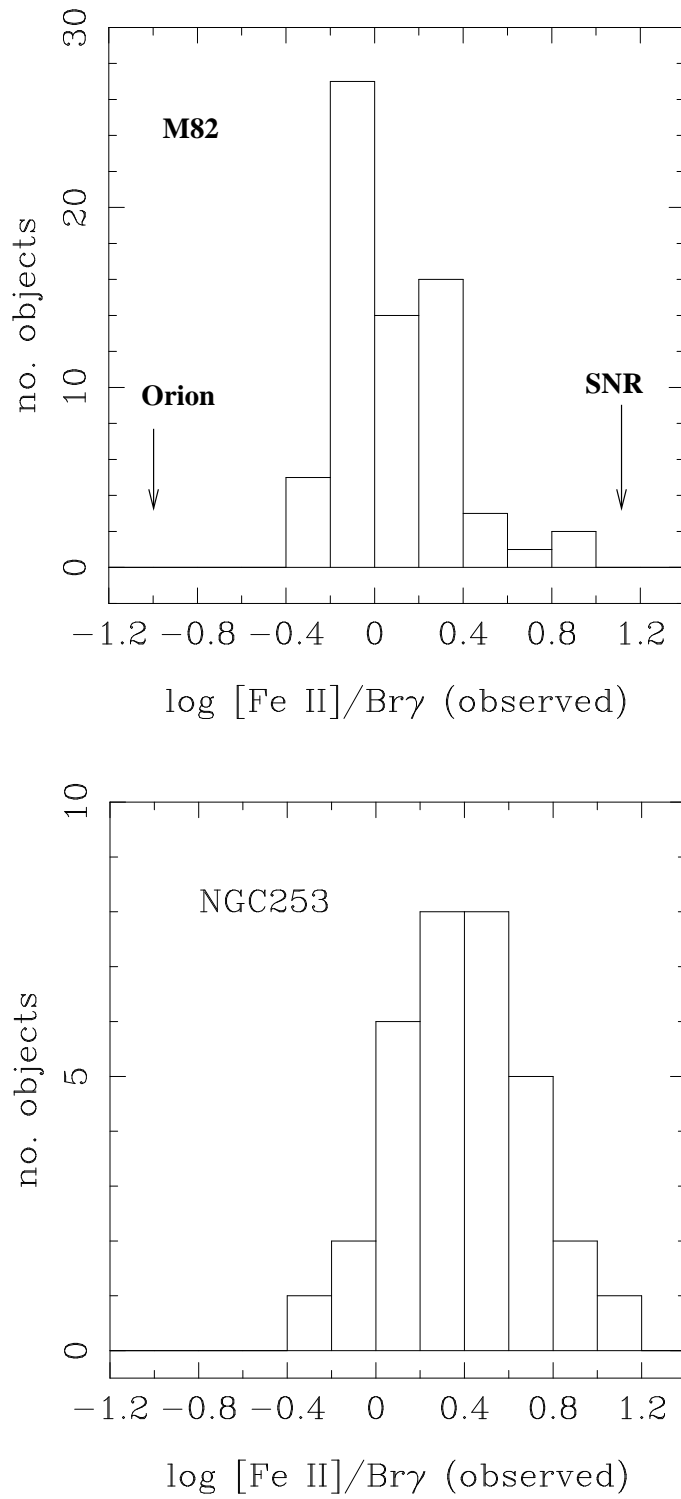


FIG. 10.— Histograms of the observed $[\text{Fe II}]_{1.644\mu\text{m}}/\text{Br}\gamma$ line ratios of the compact $[\text{Fe II}]$ sources.

This figure "figure1a.jpeg" is available in "jpeg" format from:

<http://arxiv.org/ps/astro-ph/0212142v1>

This figure "figure1b.jpeg" is available in "jpeg" format from:

<http://arxiv.org/ps/astro-ph/0212142v1>

This figure "figure2a.jpeg" is available in "jpeg" format from:

<http://arxiv.org/ps/astro-ph/0212142v1>

This figure "figure2b.jpeg" is available in "jpeg" format from:

<http://arxiv.org/ps/astro-ph/0212142v1>

This figure "figure3a.jpeg" is available in "jpeg" format from:

<http://arxiv.org/ps/astro-ph/0212142v1>

This figure "figure3b.jpeg" is available in "jpeg" format from:

<http://arxiv.org/ps/astro-ph/0212142v1>

This figure "figure4a.jpeg" is available in "jpeg" format from:

<http://arxiv.org/ps/astro-ph/0212142v1>

This figure "figure4b.jpeg" is available in "jpeg" format from:

<http://arxiv.org/ps/astro-ph/0212142v1>

This figure "figure6a.jpeg" is available in "jpeg" format from:

<http://arxiv.org/ps/astro-ph/0212142v1>

This figure "figure6b.jpeg" is available in "jpeg" format from:

<http://arxiv.org/ps/astro-ph/0212142v1>

This figure "figure7a.jpeg" is available in "jpeg" format from:

<http://arxiv.org/ps/astro-ph/0212142v1>

This figure "figure7b.jpeg" is available in "jpeg" format from:

<http://arxiv.org/ps/astro-ph/0212142v1>

This figure "figure8a.jpeg" is available in "jpeg" format from:

<http://arxiv.org/ps/astro-ph/0212142v1>

This figure "figure8b.jpeg" is available in "jpeg" format from:

<http://arxiv.org/ps/astro-ph/0212142v1>